JOURNAL OF CATALYSIS 128, 48–62 (1991)

Co-impregnated Rh/Al_2O_3

II. Nitric Oxide Reduction and SO_2 Poisoning

J. S. HEPBURN,* H. G. STENGER, JR.,* AND C. E. LYMAN†

*Department of Chemical Engineering, and †Department of Materials Science and Engineering, Lehigh University, Bethlehem, Pennsylvania 18015

Received April 16, 1990; revised August 24, 1990

In the present study, the catalytic reduction of nitric oxide by H_2 with eggshell and egg-white HF co-impregnated Rh on γ-Al_2O_3 honeycomb catalysts has been investigated to determine the effects of diffusion resistances on the rate and selectivity of the reduction reaction. Intrinsic kinetic data for NO reduction with H_2 over Rh/γ-Al_2O_3 was measured at 165°C and fit to a simplified Langmuir–Hinshelwood kinetic expression. The intrinsic kinetic model was used to develop a reactor model for NO reduction with RH/γ-Al_2O_3 honeycomb catalysts. Theoretically predicted reaction rates and selectivities for the honeycomb catalysts were found to agree closely with measured reactor performance data. Poisoning the honeycomb-supported catalysts with SO_2 showed that the eggshell and egg-white Rh catalysts deactivated at similar rates. Electron probe microanalysis (EPMA) of the poisoned catalysts revealed that sulfur was distributed throughout the support, indicating that SO_2 is not limited by diffusion in this system. Analytical electron microscopy (AEM) confirmed a high degree of S/Rh coordination within the egg-white Rh honeycomb catalyst and much less coordination of sulfur with the alumina support. This was attributed to high concentrations of fluorine (1 to 2 wt%) deposited on the support from co-impregnation with HF. This fluorine is postulated to inhibit SO_2 adsorption onto the support surface.

INTRODUCTION

The internal distribution of active components within a supported catalyst plays an important role in determining catalyst performance (i.e., activity, selectivity, and durability). Diffusional resistances result in reaction rate and concentration gradients within the support. As a result, significant modifications in catalyst performance can be achieved by manipulating the distribution of the active ingredients along the characteristic dimensions of the support (*1*). This topic was first addressed by Kasaoka and Sakata (*2*) who derived formulas for the effectiveness factor with variations in diffusivity and reaction rate constants within the support. Shortly afterward, Carberry and Minhas (*3*) discussed the advantages of nonuniform distributions of active components within the catalyst support. Prior to these early works, most heterogeneous catalytic studies were based upon uniformly active supported catalysts. The concentration profile of the active ingredients within a supported catalyst can be categorized by one of the idealized forms illustrated in Fig. 1. The shaded areas represent regions within the honeycomb support where the active ingradient is deposited. Figure 1a is a uniform internal catalyst distribution. Figure 1b is an eggshell type supported catalyst with the active material deposited at the outer surface of the support. Figure 1c shows an egg-white distribution of active component, and when the active ingredient is concentrated in the center of the support, it is referred to as an egg-yolk catalyst profile (Fig. 1d).

In the absence of poisoning or selectivity considerations, eggshell catalyst distributions are optimal for catalytic reactions which display positive-order rate dependen-

0021-9517/91 $3.00

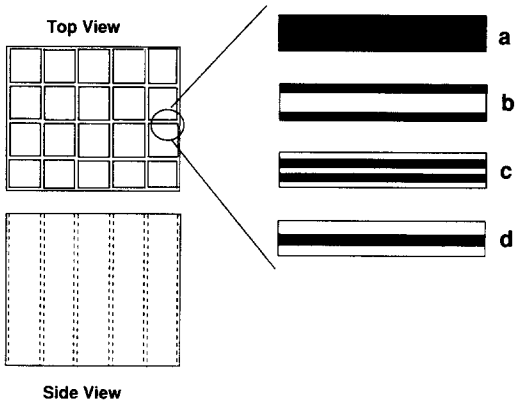

FIG. 1. Schematic representation of porous honeycomb support with (a) uniform, (b) eggshell, (c) egg-white, and (d) egg-yolk internal distributions of active ingredient.

cies upon reactant concentrations (*4*). For supported metal catalysts, however, maximum metal dispersion and resistance to sintering most often occur at the minimum concentration of the deposited metal (*5*). Therefore if diffusional resistances are not too severe, a uniform distribution of metal may be better than an eggshell distribution in catalysts of comparable metal loading (*6*).

For catalytic reactions which exhibit negative-order rate dependencies upon reactant concentration, an egg-white or egg-yolk distribution of active ingredient may be optimal. Morbidelli *et al.* (*7*) showed that the optimum catalyst activity profile for a bimolecular Langmuir–Hinshelwood reaction is given by the Dirac Delta function (i.e., an egg-white distribution of active ingredient). In addition, egg-white catalysts have been found to perform better and exhibit longer stability for automotive catalytic convertors (*8*). Wei and Becker (*9*) considered the oxidation of CO over Pt/alumina. For this reaction, which can be of negative order, an egg-yolk catalyst distribution was found to give the highest effectiveness at low temperature. In some cases, none of the idealized internal distributions of active ingredient shown in Fig. 1 are optimal. For instance, an internal distribution which decreases from the support exterior to its center has been proven to be most effective and give the highest selectivity for two consecutive first-order irreversible reactions in which the intermediate is the desired product (*10, 11*).

The optimal internal distribution of active ingredient with respect to durability depends on how a poison deposits. If the poison is not hindered significantly by mass transfer resistances, it will deposit uniformly within the support, and an eggshell catalyst will yield the best service (*12*). On the other hand, if the poison is severely hindered by diffusional resistances, it is better to use a catalyst with an egg-white or egg-yolk internal distribution because poisoning will generally start at the exterior surface of the support and proceed inward (*13, 14*). Under conditions of large Theile numbers, Bacaros *et al.* (*13*), showed that a uniform distribution may be nearly as good as the egg-yolk or egg-white catalyst.

In the present work, the catalytic reduction of NO by H_2 with eggshell and egg-white $Rh/\gamma\text{-}Al_2O_3$ honeycomb catalysts is investigated. A honeycomb reactor model which accounts for the internal distribution of deposited Rh is also presented. Theoretical predictions from this model are compared to experimentally measured reactor data. In addition, the durability of eggshell and egg-white Rh catalysts in SO_2 containing feeds is compared. The goal is to determine the role that the internal catalyst distribution plays in determining the catalytic performance of supported Rh for NO reduction by H_2, and how the distribution effects the poison resistance of the catalyst. The motivation for this work is the design of catalysts for low-temperature NO reduction in stationary sources such as power plants and industrial boilers where SO_2 poisoning is a concern.

INTRINSIC KINETICS

Experimental

A powdered Rh/γ-alumina catalyst was prepared by impregnating a finely divided γ-

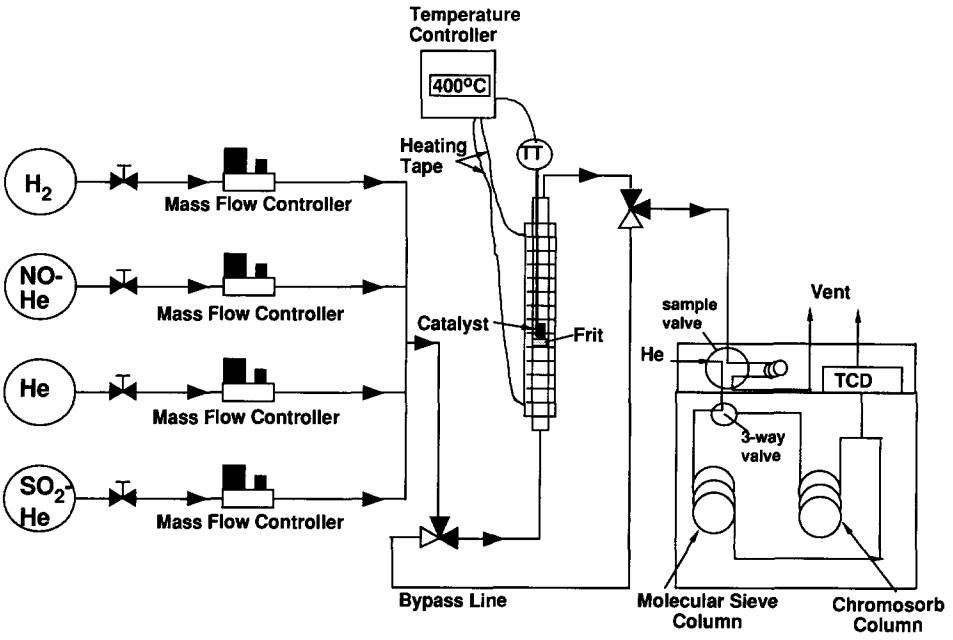

FIG. 2. Experimental apparatus for catalyst testing.

alumina powder (Corning, particle size between 25 and 50 μm) with an aqueous solution of $RhCl_3$ (Aldrich Chemical Company) to incipient wetness. The solution concentration was adjusted to yield approximately 0.1 wt% Rh on the finished catalyst. The impregnated powder was dried in air at 80°C for 1 h and calcined in air at 500°C for an additional 5 h. The catalyst was then reduced under flowing H_2 at 400°C for 20 h. A sample of the finished catalyst was dissolved in hydrofluoric acid and analyzed for Rh by atomic absorption (model 373 Perkin-Elmer spectrophotometer). It was found to contain 0.087 wt% Rh.

Kinetics of NO reduction by H_2 were measured using the apparatus shown in Fig. 2. Amounts of 5% NO in helium, 10% H_2 in helium, 1.5% SO_2 in helium, and pure helium (Linde Division, Union Carbide) are fed through separate mass flow controllers (MKS model 259B). The inlet gas composition was adjusted by diluting the reactant gases with pure helium. The central component of this system is a microreactor which consists of a $\frac{1}{2}$-in-o.d. Pyrex glass tube with a sealed porous glass frit in the center (Fisher 11-136A). The powdered catalyst is held in place using glass wool. The reactor is heated with a heating tape. The power to the tape is varied by a temperature controller (Omega CN-5000), based on the temperature signal received from a thermocouple located in the catalyst powder. This method of temperature control was able to maintain the catalyst temperature to within 1°C. Inlet and outlet gases are analyzed by gas chromatography (a Hewlett-Packard 5890 gas chromatograph with a thermal conductivity detector and Hewlett-Packard 3933 integrator). The GC-TCD was calibrated with standard gases to the limit of detectability prior to and following each run. The detectability limit with this system is approximately 30 ppm for NO. It is known that the major products formed in noble metal reduction of NO by H_2 are N_2, N_2O, NH_3, and H_2O (*15–17*). NO and N_2 are separated using a molecular sieve (5A) column while N_2O and NH_3 are separated on a Chro-

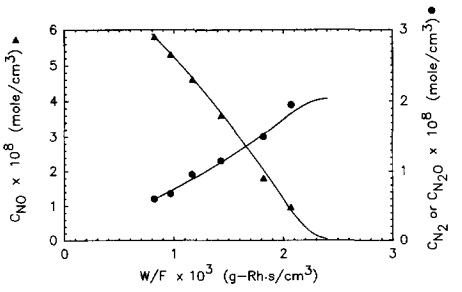

FIG. 3. Numerical fit of the reaction model with the experimental intrinsic kinetic and selectivity data. Lines are model predictions and points are data.

mosorb 103 column. The Chromosorb column was preconditioned by injecting 5 cm^3 of gaseous ammonia before each analysis. Columns in the gas chromatograph were switched manually; therefore, two samples were needed for a complete analysis of an outlet sample.

Kinetic data was measured with 0.75 g of powder catalyst at 165°C. The concentrations of NO and H_2 at the reactor inlet were 8.20×10^{-8} mol/cm^3 (3000 ppm) and 1.64×10^{-7} mol/cm^3 (6000 ppm), respectively. The reactor was operated in an integral mode. The total flow rate was varied at constant inlet conditions to obtain conversions of NO between 0 and 100%.

Results

At 165°C, the primary reactions which occur in the catalytic reduction of NO by H_2 over $Rh/\gamma\text{-}Al_2O_3$ are known to be

$$2\,NO + 2\,H_2 \rightarrow N_2 + 2H_2O \quad (1)$$

$$2\,NO + H_2 \rightarrow N_2O + H_2O \quad (2)$$

Approximately equal selectivity to N_2 and N_2O was observed for all runs, and no NH_3 was detected in the product stream. Material balances based on total nitrogen (moles N leaving reactor/moles N entering reactor) were consistently between 90 and 100%. The exiting concentrations of NO, N_2, and N_2O are shown in Fig. 3 for varying values of W/F, where W/F, a modified residence time, is the grams of Rh per cm^3/s of reactant gas flow rate.

Kinetic Model

If the rate-limiting step for the disappearance of NO and the production of N_2 and N_2O is the surface reaction of an adsorbed NO with an adsorbed H atom (*16, 17*), and if it is further assumed that product adsorption is minimal, the rate of reactions 1 and 2 can be represented by

$$r_i = \frac{k_{sr,i}K_{NO}K_{H_2}^{1/2}C_{NO}C_{H_2}^{1/2}}{(1 + K_{NO}C_{NO} + K_{H_2}^{1/2}C_{H_2}^{1/2})^2}. \quad (3)$$

If the surface coverage of NO is much greater than that of H, then

$$1 + K_{NO}C_{NO} >>> K_{H_2}^{1/2}C_{H_2}^{1/2}. \quad (4)$$

The rate of reaction i (1 or 2) then becomes

$$r_i = \frac{k_{sr,i}K_{NO}K_{H_2}^{1/2}C_{NO}C_{H_2}^{1/2}}{(1 + K_{NO}C_{NO})^2} = \frac{k_iC_{NO}C_{H_2}^{1/2}}{(1 + K_{NO}C_{NO})^2}. \quad (5)$$

The rates of NO reduction, N_2 formation, and N_2O formation can be written as: $R_{NO} = -2(r_1 + r_2)$, $R_{N_2} = r_1$, and $R_{N_2O} = r_2$. If equal selectivity to N_2 and N_2O is assumed then $k_1 = k_2$. In the past, this model has been found to accurately represent the intrinsic kinetics of NO reduction over a wide range of conditions (*15–17*).

For catalytic reactions carried out in an integral reactor with negligible heat and mass transfer resistances and negligible axial dispersion,

$$\frac{W}{F} = \int_{C_i^{in}}^{C_i^{out}} \frac{dC_i}{R_i}, \quad (6)$$

where F is the volumetric flow rate, W is the amount of Rh loaded into the reactor, and R_i is the net reaction rate of component i. This model assumes the Rh is uniformly dispersed on the alumina support. To determine the rate constants, k_1 (or k_2) and K_{NO}, the experimental data of Fig. 3 was fit by numerical integration of Eq. (6) with various trial and error values of k_1 and K_{NO}. A best

TABLE 1

Experimental Results for Catalysts I–IV

Catalyst	NO Reduction rate (μmol/s/g Rh)	Selectivity to N_2 (R_{N_2}/R_{NO})	Rhodium (wt%)
A	40.5	0.52	0.11
B	24.1	0.51	0.12
C	16.8	0.49	0.11
D	18.3	0.52	0.12

fit was obtained with $k_1 = k_2 = 1.1 \times 10^7$ ($cm^{4.5}/mol^{0.5}$-s-g Rh) and $K_{NO} = 7.8 \times 10^7$ (cm^3/mol). The experimental data is compared to the predictions of the proposed kinetic rate expression in Fig. 3.

HONEYCOMB CATALYST KINETICS

Experimental

A Rh eggshell and three Rh egg-white honeycomb catalysts were prepared by aqueous co-impregnation of $RhCl_3$ (Aldrich Chemical Company) with HF into γ-alumina honeycombs of square cell geometry (Corning Celcor EX78). Details of the preparation and characterization of these catalysts can be found in Part 1 of this work (*18*). The Rh profiles of these four catalysts are displayed in (*18*, Figs. 3–6). The catalysts are designated A, B, C, and D which correspond to the internal distributions shown in (*18*, Figs. 3–6), respectively. Each catalyst sample was a single wall from the alumina honeycomb and was cut to provide approximately 1.2 g of total catalyst. The weight percent of rhodium on each was approximately 0.1%, as determined from integrating the EPMA profile. The exact rhodium loading is listed in Table 1. All four catalysts were reduced for 20 h under flowing H_2 at 400°C prior to testing.

The kinetics of NO reduction by H_2 with catalysts A, B, C, and D were measured in the apparatus shown in Fig. 2. All four catalysts were tested at 165°C with concentrations of NO and H_2 at the reactor entrance equal to 8.2×10^{-8} (3000 ppm) and 1.64×10^{-7} mol/cm^3 (6000 ppm), respectively. In order to compare rates of NO reduction on equivalent bases, the total flow entering the reactor was adjusted to give conversions of NO approximately equal to 95%. The catalyst was assumed at steady state when the exiting concentration of NO did not change more than 2% for one hour. This typically required 2 to 3 h of reaction time.

Results

The measured kinetic data is summarized in Table 1, which shows that the eggshell Rh catalyst (catalyst A) is about two times more effective for reacting NO than the egg-white Rh catalysts (catalysts B–D). As the Rh is driven further beneath the support surface (*18*, Figs. 4–6), the rate of NO reduction first decreases (catalysts B and C) and then increases slightly (catalyst D). Within the experimental error of the analysis, the selectivity to N_2 and N_2O was observed to be approximately equal for all four catalysts. As was found previously with the powdered $Rh/\gamma\text{-}Al_2O_3$ catalyst, no NH_3 was detected in the reactor outlet.

Honeycomb Reactor Model

Under steady-state isothermal conditions, the rate of NO removal and the rate of N_2 and N_2O formation in the square channels of the honeycomb are governed by

$$F\frac{\partial C_i}{\partial z} = 4Hk_{m,i}(C_i - C_i^{wall}(x = l)), \quad (7)$$

where H is the width of a single channel and $4H$ is the wetted perimeter of the channel (see Appendix for other symbol definitions). The modeling geometry is described in Fig. 4. Equation (7) assumes that the gases within a channel are well mixed in the x direction and plug flow axially. Equation (7) has a boundary condition at the entrance to the honeycomb of

$$C_i = C_i^{in}, \quad \text{at } z = 0, \quad (8)$$

where C_i^{in} is the concentration of i entering the reactor. The concentration of i at the external surface of the honeycomb wall

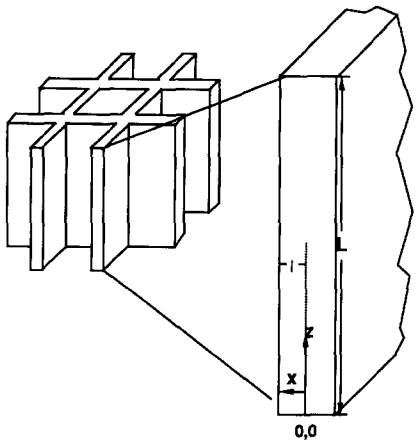

FIG. 4. Coordinate system for honeycomb reactor model.

(C_i^{wall} (at $x = l$)), is governed by reaction and diffusion within the support

$$D_{e,i}\frac{\partial^2 C_i^{wall}}{\partial x^2} = g(x)R_i(x), \qquad (9)$$

where $g(x)$ is the weight of deposited Rh per unit pore volume and is obtained directly from the internal distribution of deposited Rh shown in (*18*, Figs. 3–6). $R_i(x)$ is the local rate of reaction for species i and is a function of $C_{NO}^{wall}(x)$ and $C_{H_2}^{wall}(x)$. This model assumes that the Rh dispersion is independent of location within the support. At the low metal loadings present on these catalysts, this assumption is reasonable. The boundary condition at the outer surface of the wall (at $x = l$) is obtained by equating the diffusive flux within the support wall to the mass transfer rate at the external surface of the wall.

$$D_{e,i}\frac{\partial C_i^{wall}}{\partial x} = -k_{m,i}(C_i - C_i^{wall}), \quad \text{at } x = l, \qquad (10)$$

A solution to Eq. (9) must also meet a condition of symmetry at the center of the support ($x = 0$):

$$\frac{\partial C_i^{wall}}{\partial x} = 0, \quad \text{at } x = 0. \qquad (11)$$

Equations (7) and (9) were solved numerically by a first-order finite difference algorithm. Numerical regression to obtain the best values for $k_{m,i}$ and $D_{e,i}$ was performed by a trial and error procedure. The external mass transfer coefficient, $k_{m,i}$, could not be calculated accurately from literature correlations because of the uncertainty in the velocity at the catalyst surface due to the way the catalyst was held in the reactor. Because internal diffusion resistances are relatively unimportant for the eggshell Rh catalyst, $k_{m,NO}$ was obtained by fitting the eggshell catalyst (catalyst A) kinetic data. The other mass transfer coefficients for the other species were calculated from the NO value by assuming they are proportional to the square root of their gas phase diffusivities (see Eq. (12)). Then, holding $k_{m,i}$'s constant, the effective diffusivity of NO within the support wall, $D_{e,NO}$, was adjusted to obtain the best fit to the remaining egg-white catalyst (catalysts B–D) data. For each assumed value of $D_{e,NO}$, the remaining effective diffusivities were calculated in the following manner.

From the Chapman–Enskog kinetic theory of gases (*19*), the binary diffusivity of species i in helium can be calculated using Eq. (12).

$$D_{i,He} = 0.001853\frac{\sqrt{T^3((1/M_i) + (1/M_{He}))}}{\sigma_{i,He}^2\Omega_{D,i,He}}. \qquad (12)$$

Using Eq. (12), the diffusivities of NO, H_2, N_2, and N_2O in helium at 165°C are 1.27, 3.01, 1.32, and 1.13 cm^2/s, respectively. Also from the kinetic theory of gases, the Knudsen diffusivity is formulated as (*20*)

$$D_{K,i} = \frac{4}{3}r_p\left(\frac{2}{\pi}\frac{R_{gas}T}{M_i}\right)^{1/2}, \qquad (13)$$

where r_p is the average pore radius. The Knudsen diffusivities of NO, H_2, N_2, and N_2O with 4.0-nm pores (*18*) are 0.0148, 0.0574, 0.0153, and 0.0122 cm^2/s, respectively. These two types of diffusion can be combined (*20*) to determine the overall diffusivity of each species.

TABLE 2

Comparison of Predicted and Experimental Results

Catalyst	R_{NO}^{exp} (μmol/s/g Rh)	R_{NO}^{pre} (μmol/s/g Rh)	$S_{N_2}^{exp}$	$S_{N_2}^{pre}$
A	40.5	40.0	0.52	0.50
B	24.1	23.5	0.51	0.50
C	16.8	17.0	0.49	0.50
D	18.3	18.5	0.52	0.50

$$\frac{1}{D_i} = \frac{1}{D_{i,\mathrm{He}}} + \frac{1}{D_{\mathrm{K},i}}. \tag{14}$$

Using Eq. (14) D_{NO}, D_{H_2}, D_{N_2}, and D_{N_2O} are calculated to be 0.0146, 0.0563, 0.0151, and 0.0121 cm^2/s, respectively. Finally these overall diffusion coefficients are corrected for porosity, ε, and tortuosity, τ (*20*):

$$D_{e,i} = \frac{\varepsilon}{\tau} D_i. \tag{15}$$

The porosity, ε, of the support reported by the manufacturer is 0.63 (*18*). The tortuosity, τ, is unknown; however, if we assume the tortuosity is not a function of diffusing species then

$$\frac{D_{e,i}}{D_{e,NO}} = \frac{D_i}{D_{NO}}. \tag{16}$$

Therefore by choosing $D_{e,NO}$, all other effective diffusivities can be calculated. A best fit to the experimental data in Table 1 was obtained with $k_{m,NO}$ = 0.25 cm/s and $D_{e,NO}$ = 6.25 × 10^{-3}cm^2/s, which gives a tortuosity for the alumina of 1.48. Predicted rates and selectivities are compared to the experimental kinetic data of catalysts A–D in Table 2. The honeycomb model predicts the experimentally measured rates of NO reduction quite well. The model even predicts the slight increase in R_{NO} observed with catalyst D.

Discussion

Since the honeycomb model does predict the kinetic data well, it is instructive to examine some of the numerical results which can lend insight into the processes taking place between the reactor entrance and exit. Figure 5 is a plot of the integrated NO reduction rate progressing axially along the honeycomb. Initially, the eggshell catalyst (catalyst A) is not as effective in removing NO as the egg-white catalysts (catalysts B–D), because near the inlet of the reactor (low values of z/L), the rate of NO reduction is negative order in C_{NO} (Eq. (5)). However as the concentration of NO is reduced, the $K_{NO}C_{NO}$ term in the denominator of Eq. (5) becomes less than 1, and the rate of NO reduction becomes positive order in C_{NO}. When the rate is positive order in C_{NO} (i.e., at larger values of z/L), diffusional resistances cause the egg-white catalysts (catalysts B–D) to become less effective for removing NO.

Figure 6 shows the NO concentration profiles within catalyst B, together with the rhodium profile for half of the catalyst wall. At regions near the center of the support (x/l = 0) there is no deposited Rh and no reaction taking place; therefore, the profile is flat as required by Eq. (9). The concentration of NO then increases at the peak region of the support. First the gradient in C_{NO} increases at the sharp inner side of the Rh peak and then decreases as the concentration of deposited Rh gradually falls on the outer side of the peak. In the exterior regions of the support, there is a constant slope because there is a nearly constant concentration of deposited Rh. The internal profile of C_{NO} for catalysts C and D are qualitatively very similar to those shown in Fig. 6.

Plots of the local rate of NO reduction within catalyst B at various distances along the length of the catalyst are shown in Fig. 7. The rate profiles for z/L = 0 are seen to rise from the support surface to its interior (i.e., from $x = l$ to x = 0). At the entrance to the reactor (z = 0) the rate increases with depth gradually between x/l = 1 and 0.65. Within this region, the rhodium loading is essentially constant; therefore the increased rate is due to the slight negative-order rate dependence on C_{NO}. The rate profile for z/L

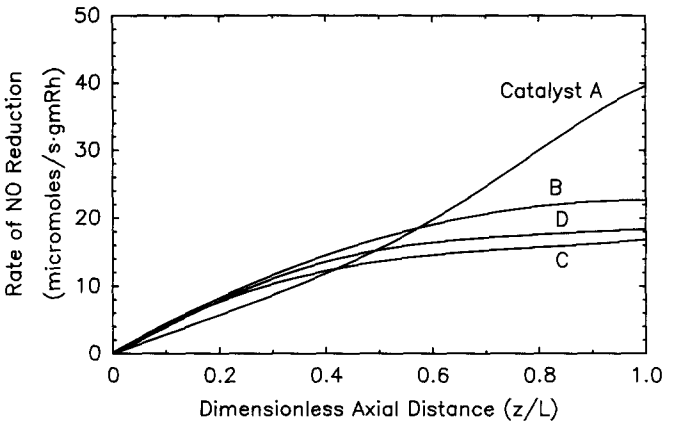

FIG. 5. Integral rate profiles of NO reduction for catalysts A–D.

= 0.25 is nearly flat in the exterior regions of the support indicating that the rate of NO reduction is close to 0^{th} order with respect to C_{NO} in this region. At all values of z/L, the interior regions of the support display two humps in the rate profiles. These two humps are caused by the shape of the rhodium distribution. Examining the rhodium distribution closely shows that there is a gradually increasing part section and then a sharp increasing section. These two regions of increasing rhodium concentration give rise to the two maxima in activity at x/l of 0.55 and 0.45. Plots of the local rate of NO reduction for catalysts C and D are qualitatively very similar to Fig. 7.

DEACTIVATION BY SO_2

Experimental Results

Two catalysts used in the preceding runs (catalysts A and B) were subjected to poisoning following the measurement of their

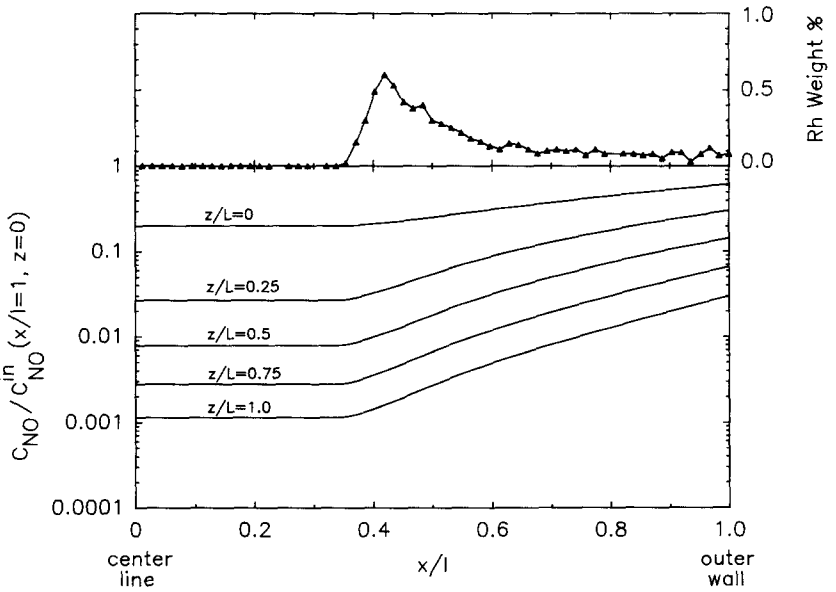

FIG. 6. Profiles of C_{NO} within catalyst B, superimposed is the rhodium distribution.

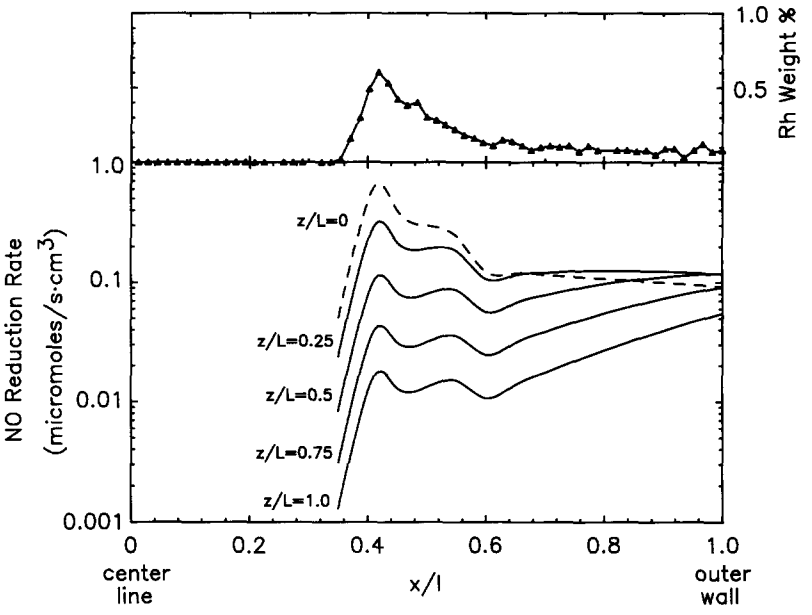

FIG. 7. Profiles of the rate of NO reduction within catalyst B.

steady-state activity. Since the rhodium is more accessible in catalyst A, it might be expected that it would poison faster. This would be caused by both diffusional limitations and adsorption of SO_2 onto the alumina in the outer regions of catalyst B. Each catalyst was poisoned at 165°C by adding SO_2 to the feed gas at a concentration of 1000 ppm. The rate of deactivation was measured with the apparatus shown in Fig. 2. The concentrations of NO and H_2 at the reactor entrance were 8.2×10^{-8} mol/cm³ (3000 ppm) and 1.64×10^{-7} mol/cm³ (6000 ppm), respectively. Prior to the introduction of SO_2 into the feed gas, the total flow of reactants was adjusted to give steady-state conversions of NO as close to 95% as possible. The steady-state activities are those given in Table 2.

Figure 8 shows the deactivation by SO_2 of the eggshell (catalyst A) and the egg-white (catalyst B) $Rh/\gamma\text{-}Al_2O_3$ honeycomb catalysts. Time values less than 0 min are shown to indicate the stability of the unpoisoned catalyst. Figure 8 shows that both catalysts deactivate at nearly the same rate. For both catalysts, the conversion of NO falls to approximately 10% in about 4 h after the introduction of SO_2 into the reactor feed. Four hours of SO_2 at 1000 ppm corresponds to 20.1 mol of SO_2 fed to the reactor per mole of rhodium present. Using the manufacturer's measured surface area for the alumina (185 m²/gm) the sulfur exposure after 4 h would be 1.05 μmol of S/m². If SO_2 were to closely pack on the alumina surface the coverage would be approximately 10 μmol/m². The poisoning was found to be irreversible at this temperature with no measurable increase in activity after removing SO_2 from the feed gas. From these experiments it is evident that there is no enhancement of the catalyst's durability by driving the Rh beneath the external surface of the support.

EPMA of Poisoned Catalysts

After poisoning, catalysts A and B, were sectioned and prepared for analysis using the electron microprobe as described previously (*21*). Rhodium, aluminum, and sulfur traces were taken across each catalyst wall. A polished iron sulfide rod (Aldrich Chemical Company) was employed as the sulfur standard. The $K\alpha$ line of sulfur was analyzed by WDS with a PET crystal. All other details of the microanalysis can be

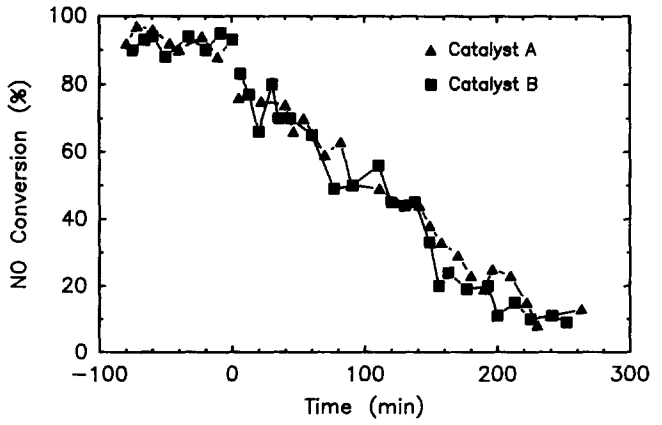

FIG. 8. Deactivation of catalysts A and B by SO_2.

found in a previous paper (*21*). The internal distributions of sulfur and rhodium within the eggshell catalyst (catalyst A) are shown in Fig. 9. The EPMA data reveals a high concentration of sulfur at the external surface of the support, with the weight ratio of rhodium to sulfur being approximately 2.5 to 3 which is a corresponding atomic ratio of 0.75 to 1.0, rhodium to sulfur. Internally, there is a uniform coverage of sulfur of approximately 0.1 wt%, which if completely on the alumina surface would correspond to a loading of 0.17 μmol/m^2 of alumina. Since only ppm sulfur impurities in the alumina are reported by the manufacturer, this sulfur must be attributed to the SO_2 poisoning.

Because catalysts A and B both poisoned at identically the same rates, it is apparent that no diffusional or adsorptive resistance was offered by the egg-white catalyst preparation (catalyst B). The internal distribution of deposited sulfur and rhodium within the egg-white catalyst (catalyst B) is shown in Fig. 10. This profile reveals a high concentration of sulfur located at the external regions of the support. The weight ratio of sulfur to rhodium at the outer wall is 4.2, or an atomic ratio of 13.5 S/Rh. Internally, the sulfur distribution closely correlates with rhodium. Peaks at 0.25 mm from the catalyst center for sulfur and rhodium have a weight ratio of 3.1 rhodium to sulfur, which corre-

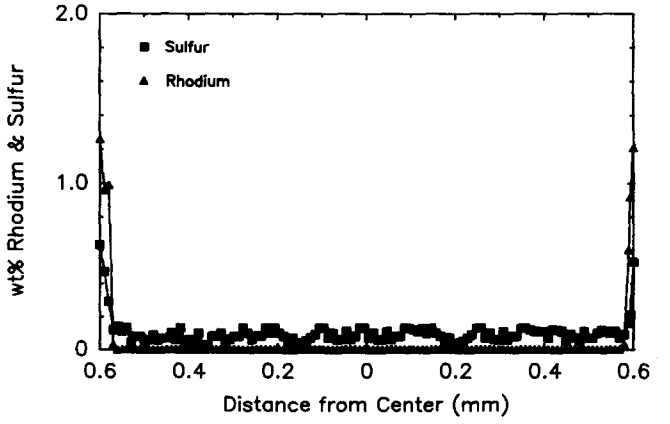

FIG. 9. Internal distribution of sulfur within poisoned catalyst A.

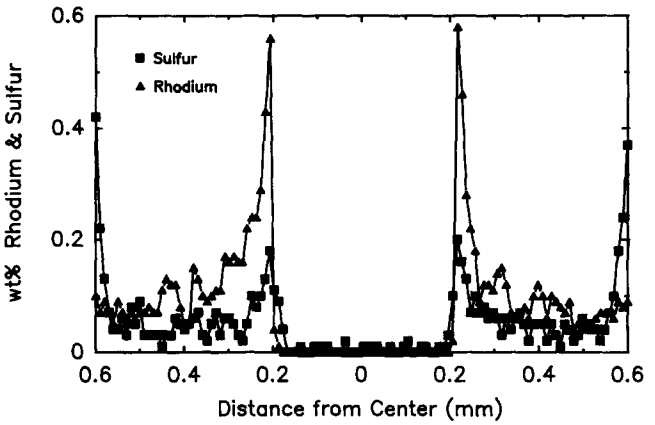

FIG. 10. Internal distribution of sulfur within poisoned catalyst B.

sponds to an atomic ratio of 0.97 Rh/S. Even though this would suggest that sulfur and rhodium may be highly coordinated throughout the catalyst, the EPMA is not capable of determining how much sulfur is coordinated with the alumina and how much is coordinated with the rhodium.

Analytical Electron Microscopy (AEM of Catalyst II)

A sample from the peak region of catalyst B was removed and placed on a carbon-coated grid (Ted Pella Inc. #T400). X-ray emission spectroscopy (XES) and high-resolution digital X-ray mapping of this sample was performed in a dedicated scanning transmission electron microscope (STEM) (Vacuum Generators HG-501 FEG STEM with a Link Systems LZ5 windowless Si/Li X-ray detector).

Figure 11 shows two 3 to 4-nm rhodium particles in the rhodium $L\alpha$ digital X-ray image. Also shown are two highly concentrated areas of sulfur in the sulfur $K\alpha$ X-ray image. These regions of sulfur correspond exactly with the locations of the rhodium particles. This shows a high degree of coordination between sulfur and rhodium for catalyst B. This is also demonstrated by the two EDS spectra shown in Figs. 12 and 13. With the electron beam of the AEM (estimated to be 1.2 nm in diameter at full width of half maximum) positioned onto one of the rhodium particles of Fig. 11, Fig. 12 shows that both the $L\alpha$ X-ray line of rhodium and the $K\alpha$ X-ray line of sulfur are clearly visible in the spectrum. With the electron beam placed off the rhodium particle (i.e., on the alumina matrix) Fig. 13 shows that there is no evidence of sulfur in the spectrum.

The EPMA fluorine profile of the poisoned catalyst B is shown in Fig. 14. This analysis shows that a large amount of fluorine is present (as much as 2 wt%), indicating that the fluorine residual left from the co-impregnation process is highly stable, even after drying, calcination, reduction, reaction, and poisoning. Details of the analysis for fluorine can be found in a previous paper (*21*). In other work in our laboratory it has been determined that fluorine, when deposited onto the surface of γ-alumina, severely inhibits the adsorption of SO_2 (*22*). This is most likely the reason for sulfur being strongly associated with rhodium rather than with the alumina in the egg-white catalyst (catalyst B) and the inability of the alumina to reduce the rate of deactivation for catalyst B over catalyst A.

CONCLUSIONS

The catalytic reduction of NO by H_2 with $Rh/\gamma\text{-}Al_2O_3$ honeycomb catalysts provides an interesting and practical system for

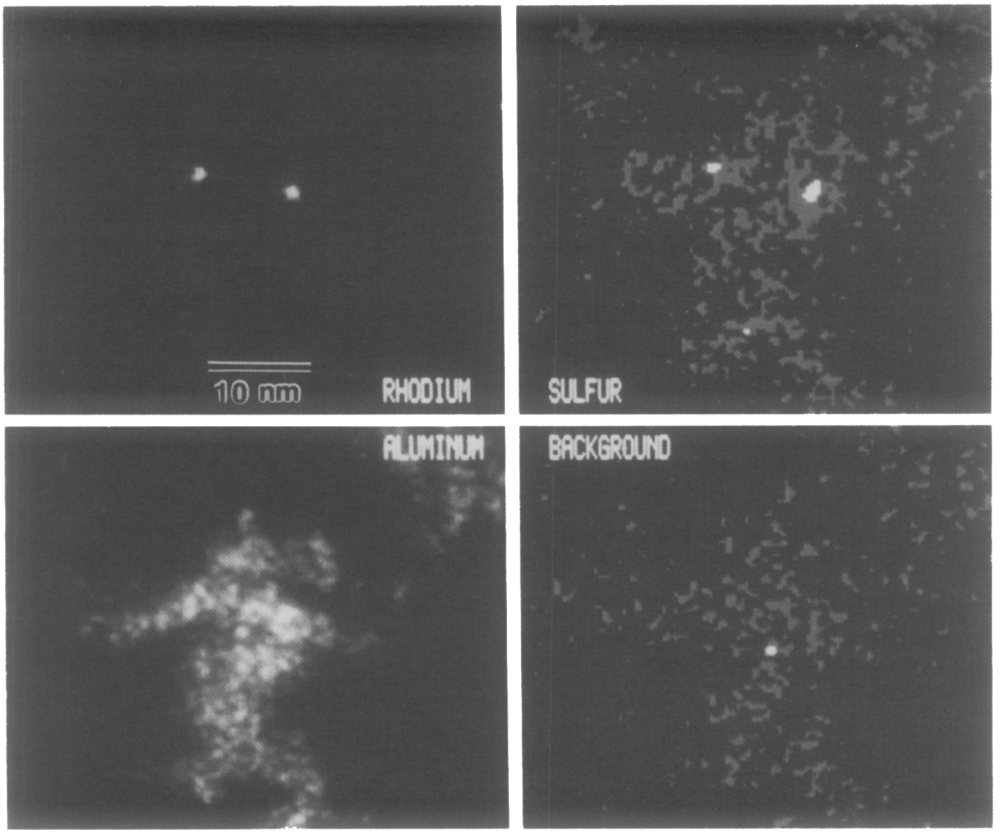

FIG. 11. Digitized X-ray emission images of elemental distributions in alumina particle removed from peak region of poisoned catalyst B (BG = background X-ray map).

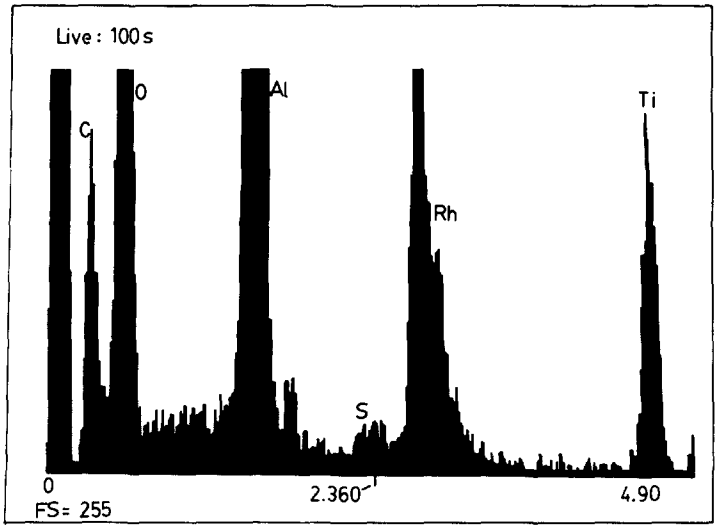

FIG. 12. EDS spectrum with electron beam positioned on a rhodium particle.

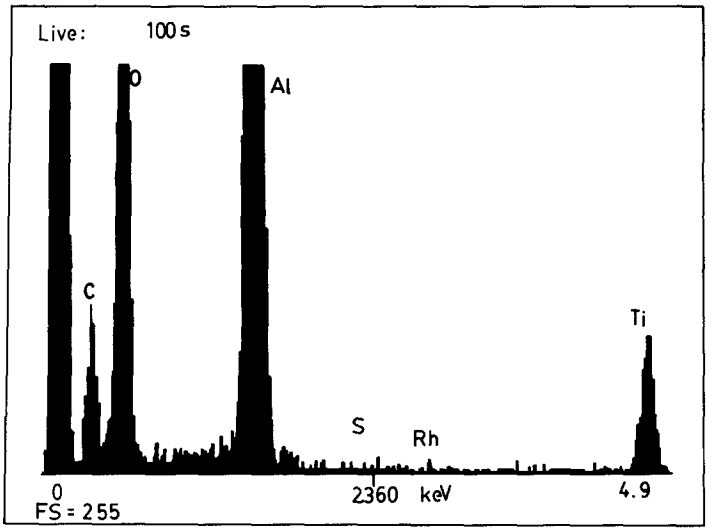

FIG. 13. EDS spectrum with electron beam positioned off of a rhodium particle.

studying diffusional and adsorptive resistances and their effect on catalyst activity, selectivity, and durability. Intrinsic kinetics of NO reduction by H_2 over finely divided $Rh/\gamma\text{-}Al_2O_3$ at 165°C were found to fit a simplified Langmuir–Hinshelwood kinetic model which assumes the rate-limiting step was the surface reaction of an adsorbed NO molecule with an adsorbed H atom. The main reactant products were found to be N_2 and N_2O which were produced at nearly equal rates. No NH_3 was detected in the product stream and nitrogen material balances were between 90 and 100%. The intrinsic kinetic model was used to develop a reactor model for NO reduction with eggshell and egg-white rhodium on alumina honeycomb catalysts. Theoretically predicted rates of NO reduction and reaction selectivities agreed closely with experimental kinetic data from four different honeycomb catalysts. At high concentrations of NO (near the reactor inlet), the egg-white catalysts were found to be most effective. At low concentrations of NO (near the reactor outlet), eggshell Rh profiles were found to outperform egg-white catalyst profiles. This was attributed to the intrinsic kinetics of NO reduction showing both a positive- and a negative-order rate dependence on NO concentration.

Sulfur poisoning with SO_2 of the rhodium on alumina honeycomb catalysts revealed several important processes. Eggshell and egg-white Rh honeycomb catalysts were found to deactivate at nearly identical rates when SO_2 was present in the reactor feed gas. EPMA of the poisoned catalysts showed that SO_2 was most likely not limited by diffusion and had no difficulty in penetrating the support interior. EPMA and

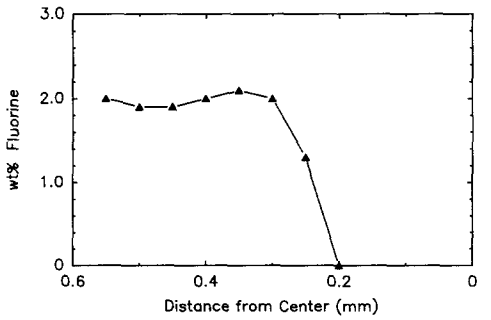

FIG. 14. Internal distribution of fluorine within poisoned catalyst B.

AEM found a high degree of coordination between sulfur and rhodium within the egg-white catalyst and showed approximately an equimolar loading of sulfur and rhodium in the poisoned catalyst. The lack of sulfur on the alumina is attributed to high concentrations of fluorine which was present on the alumina from the co-impregnation with HF. It is postulated that the fluorine inhibits the adsorption of SO_2 onto the alumina surface.

APPENDIX: NOMENCLATURE

C_i—Concentration of species i (mol/cm^3)
C_i^{in}—Concentration of i entering reactor (mol/cm^3)
C_i^{wall}—Concentration of i in the pores of the honeycomb wall (mol/cm^3)
$D_{e,i}$—Effective diffusivity of i (cm^2/s)
$D_{i,j}$—Binary gas phase difusivity of i in j (cm^2/s)
D_i—Average diffusivity within a pore (cm^2/s)
$D_{K,i}$—Knudsen diffusivity of i (cm^2/s)
F—Volumetric flow rate at operating temperature and flow rate per channel (cm^3/s)
H—Width of a honeycomb channel (cm)
k_i—Effective rate constant for reaction i (cm$^{4.5}$moles of $i^{-0.5}$/s-g of Rh)
$k_{sr,i}$—Surface reaction rate constant of reaction i (moles of i/s-g of Rh)
$k_{m,i}$—Mass transfer coefficient for species i (cm/s)
K_i—Equilibrium adsorption constant for species i (cm^3/mol)
l—Distance from support center to external surface (cm)
L—Axial length of honeycomb (cm)
M_i—Molecular weight of species i (g/mol)
r_i—Rate of reaction i (mol/s-g of Rh)
r_p—Pore radius (cm)
R_i—Reaction rate of species i (moles of i/s-g of Rh)
R_{gas}—Gas constant (8.314×10^7 dyn/mol-K)
$S_{N_2}^{exp}$—Experimental selectivity to nitrogen
$S_{N_2}^{pred}$—Predicted selectivity to nitrogen
T—Temperature (K)
W—Weight of rhodium (g)
x—Distance from center of honeycomb wall (cm)
z—Distance from entrance of reactor (cm)

Greek

ε—Porosity
σ—Leonard–Jones force constant (Å)
τ—Tortuosity
Ω_D—Collision integral

ACKNOWLEDGMENTS

This work was supported by the Department of Energy under contract DE-FG02-86ER45269 and by the Pennsylvania Energy Development Authority. Also, thanks is given to Corning for the donation of the γ-alumina honeycombs.

REFERENCES

1. Hegedus, L. L., and McCabe, R. W., *Catal. Rev. Sci. Eng.* **23,** 377 (1981).
2. Kasaoka, S., and Sakata, Y., *J. Chem. Eng. Japan.* **1,** 138 (1968).
3. Carberry, J. J., and Minhas, S., *J. Catal.* **14,** 270 (1969).
4. Becker, E. R., and Nutall, T. A., *in* "Preparation of Catalysts II, Studies in Surface Science and Catalysis" (B. Delmon, P. Grange, P. Jacobs, and G. Poncelet, Eds.), Vol. 3, p. 159. Elsevier, Amsterdam, 1979.
5. Benesi, H. A., Curtis, R. M., and Struder, H. P., *J. Catal.* **10,** 328 (1968).
6. Roth, J. F., and Richard, T. E., *J. Res. Inst. Catal.* **20,** 85 (1972).
7. Morbidelli, M., Serrida, A., and Varma, A., *Ind. Eng. Chem. Fundam.* **21,** 278 (1982).
8. Michalko, E., U.S. Patent 3,259,589, July 1966.
9. Wei, J., and Becker, E. R., *J. Catal.* **46,** 365 (1977).
10. Yazdi, F. S., and Petersen, E. E., *Chem. Eng. Sci.* **27,** 277 (1972).
11. Corbett, W. E., and Luss, D., *Chem. Eng. Sci.* **29,** 1573 (1974).
12. Becker, E. R., and Wei, J., *J. Catal.* **46,** 372 (1977).
13. Bacaros, T., Bebelis, S., Pavlou, S., and Vayenas, C. G., "Catalyst Deactivation." Elsevier, Amsterdam, 1987.
14. Lee, S. Y., and Aris, R., *Catal. Rev. Sci. Eng.* **27,** 207 (1985).
15. Hecker, W. C., and Bell, A. T., *J. Catal.* **84,** 200 (1983).
16. Hecker, W. C., and Bell, A. T., *J. Catal.* **92,** 247 (1985).

17. Stenger, H. G., and Hepburn, J. S., *Energy Fuels* **1,** 412 (1987).
18. Hepburn, J. S., Stenger, H. G., and Lyman, C. E., *J. Catal.* **128,** (1991).
19. Bird, B. R., Stewart, W. E., and Lightfoot, E. N., "Transport Phenomena," Vol. 1. Wiley, New York, 1960.
20. Froment, G. F., and Bischoff, K. B., "Chemical Reactor Analysis and Design," Wiley, New York, 1979.
21. Hepburn, J. S., Stenger, H. G., and Lyman, C. E., *Appl. Catal.* **55,** 271 (1989).
22. Meyer, E. C., PhD dissertation, Lehigh University, October 1989.